Determination of the geometric parameters of the defects based on the tomographically obtained data and their influence on the fatigue behavior of the S960 with laser cladded protective layers

Pavel Doubek
Brno University of Technology, Faculty of Civil Engineering, Institute of Structural Mechanics, Veveří 331/95, 602 00 Brno, Czech Republic, and OMNI-X CZ s.r.o., Samalova 60a, 615 00 Brno, Czech Republic
pavel.doubek@omni-x.cz http://orcid.org/0000-0002-3010-8771

Ivana Kumpová
Brno University of Technology, Faculty of Civil Engineering, Veveri 331/95, 602 00 Brno, Czech Republic and Institute of Theoretical and Applied Mechanics of the Czech Academy of Sciences, v. v. i, Prosecka 76, Praha, 190 00, Czech Republic
Ivana.Kumpova@vutbr.cz, https://orcid.org/0000-0001-8556-4996

Lucie Malíková, Mohammad Sami Al Khazali, Stanislav Seitl
Czech Academy of Sciences, Institute of Physics of Materials, v. v. i., Žižkova 22, 616 00 Brno, Czech Republic, and Brno University of Technology, Faculty of Civil Engineering, Veveří 331/95, 602 00 Brno, Czech Republic
Lucie.Malikova@vut.cz, http://orcid.org/0000-0001-5868-5717
Mohammad.Sami.Al.Khazali@vutbr.cz, https://orcid.org/0009-0004-6998-9264
seitl@ipm.cz, http://orcid.org/0000-0002-4953-4324

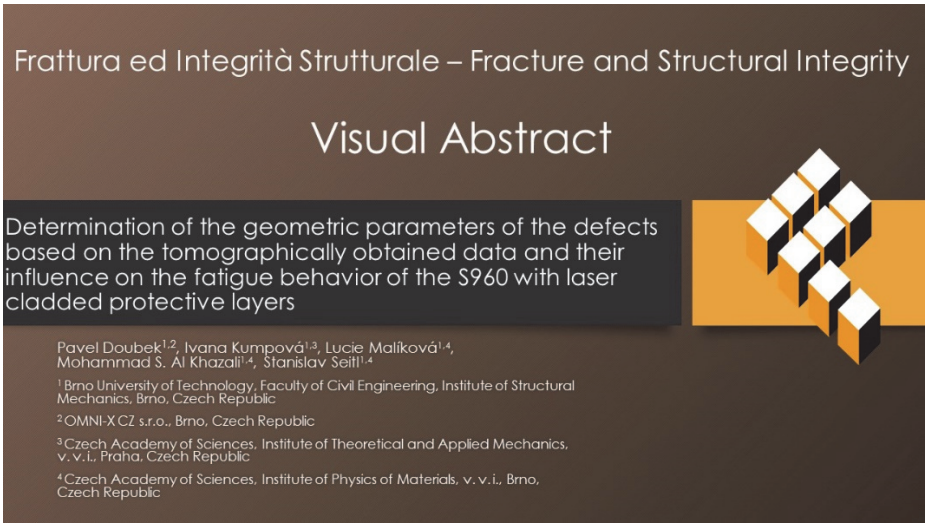

KEYWORDS. S960, Tomography, Laser cladded, Aluminum bronze, Cobalt alloy, stainless steel.

Citation: Doubek, P., Kumpová, I., Malíková, L., Al Khazali, M.S., Seitl, S., Determination of the geometric parameters of the defects based on the tomographically obtained data and their influence on the fatigue behavior of the S960 with laser cladded protective layers, Fracture and Structural Integrity, 71 (2025) 67-79.

Received: 06.09.2024
Accepted: 07.10.2024
Published: 11.10.2024
Issue: 01.2025

INTRODUCTION

The use of laser cladding technology has many indisputable technological and economic advantages [1-3]. A suitably chosen combination of base material and surface layer enables to achieve the required properties of the product [4-6]. Using laser technology to melt and fuse metal powders onto the surface of metal parts, it is capable of producing high-quality coatings with minimal distortion and waste. However, its application to the base material significantly affects the mechanical properties of such a product due to the thermal effect during cladding process. Inhomogeneities in the material structure of the surface layer and the formation of a heat-affected zone (HAZ) influence the fatigue life of laser-cladded components [7]. It can be used to repair damaged parts, enhance wear resistance, and even create new parts with complex geometries.

The fatigue behaviour of a material can also be significantly changed by the existence of geometrical flaws [8]. Nevertheless, the fatigue strength is no longer impacted by the flaw when the defect size is sufficiently small, that is, below a critical value. One way to understand the so-called Kitagawa effect is as a struggle between fracture initiation mechanisms that are controlled by the defect or the microstructure.

This work follows on from the analysis of the fatigue behavior of the S960 with laser cladded protective layers by a three-point bending test. The article presents the experimental results of a series of tomographic measurements of samples and data processing in the meaning of defectoscopy, segmentation and determination of geometric parameters of structural defects (non-integrities) in the functional protective layer, e.g. [9, 10]. Knowledge of the parameters of these defects (stress concentrators) is used as one of the inputs into the model for assessment of the effect of such defects on the fatigue parameters of bi-material components created by the laser cladding technology during the three-point bending test.

MATERIAL PROPERTIES AND GEOMETRY OF THE SPECIMENS

The tested samples consist of high strength steel S960 [11] to which a four different types of surface layers using robotic laser cladding device MLHW-4000 with the diode source are applied [12]. The final samples were cut out from cladded plates perpendicularly to the cladding direction and machined to final dimensions. The surface of the cladded layer was machined with a roughness of Ra 0.4. The parameters of the samples are given in Tabs. 1–2 and Fig. 1. The added metal was cladded in two overlapping layers (coatings) as shown schematically in Fig. 2.

Designation	Description	E [GPa]	ν [-]	Hardness HV 0.5
S960	High strength steel	202	0.27	346
Metco 51NS	Aluminum bronze	117	0.32	158
Rockit 401	Hard chrome	104	0.22	620
Not public	Cobalt alloy	214	0.27 – 0.30	440
Höganäs 316L	Stainless steel	193	0.25	155

Table 1: Basic parameters of material of the substrate and laser-cladded layers.

Sample No.	Material	l [mm]	W [mm]	B [mm]	t [mm]
B9/17	Aluminium-Bronze/S960	100.0	22.42	5.57	1.77
T34	Hard chrome/S960	100.0	20.51	5.59	0.76
ST9/14	Cobalt alloy/S960	100.0	21.21	5.54	0.82
N9/17	Stainless steel/S960	100.0	21.42	5.44	0.98

Table 2: Identification and parameters of samples for tomographic measurements.

As shown in Fig. 3, the geometric dimensions of the single-track deposition region mainly include W (deposition width), H (deposition height), and h (remelting depth), which are obtained by using Photoshop's measurement tool. The geometric dilution ratio (D) was defined as [13]:

$$D = \frac{h}{(H + h)} \tag{1}$$

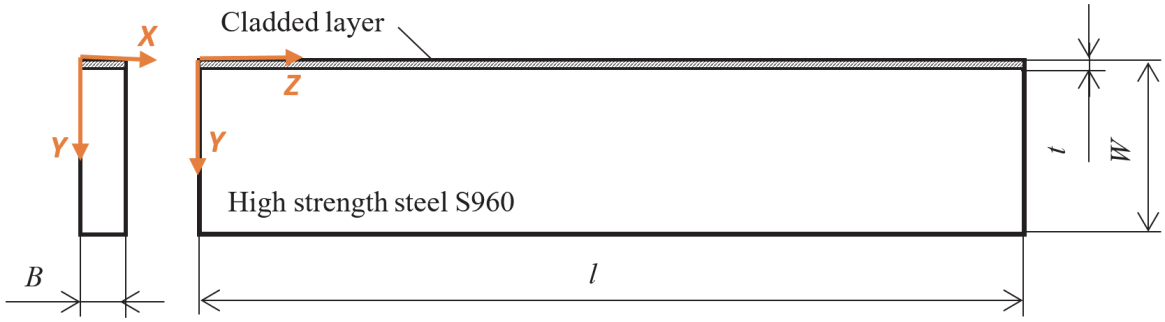

Figure 1: Schematic illustration of the shape and basic dimensions of the tested samples

.

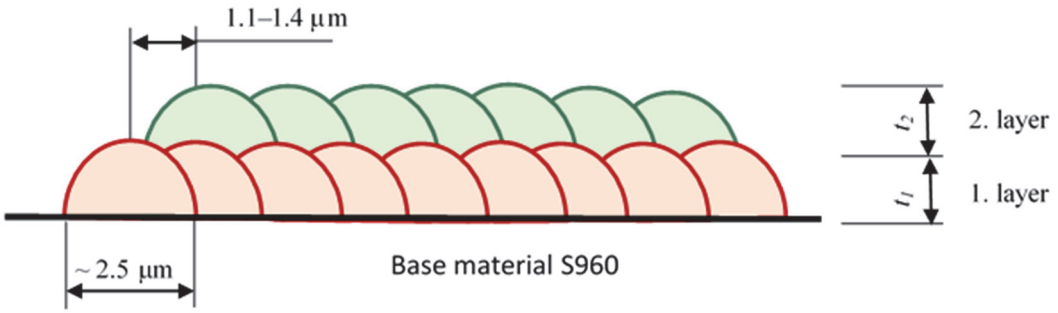

Figure 2: Schematic illustration of cladding in section along the height of the sample.

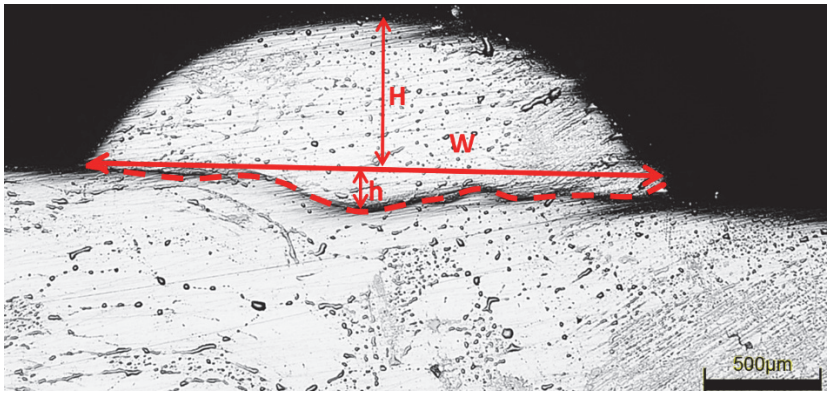

Figure 3: Geometric dimensions of the single-track deposition region of Aluminium-Bronze/S960.

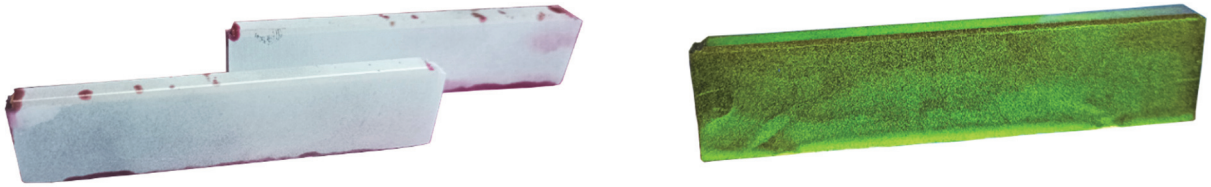

Figure 4: Example of the non-destructive detection of the open surface cracks and non-solids in the aluminium bronze/S960 samples; (a) Dye Penetrant Crack test with indicated surface defects; (b) Magnetic Particle inspection

In case of Aluminium-Bronze/S960, the dimension is W=2513 µm, H=653 µm and h=180 µm, the geometric dilution ratio D=0.21 (21%), see Fig. 3. It is the optimum parameter for laser cladded surface [14].

The X-ray fluorescence spectrometry (XRF spectrometry) was performed with the Delta Professional handheld spectrometer to identify the actual chemical composition of the cladded layers [15, 16]. The results for each coating material and parameters of deposition are described in detail [7, 17].

DETECTION OF OPEN SURFACE DEFECTS/CRACKS IN THE LASER CLADDED LAYERS

Two independent non-destructive methods were used to detect open surface cracks and discontinuties of the cladded layers, see Fig. 4. The Dye Penetrant Crack test was performed according to EN ISO 3452-1 and EN ISO 23277. The method is based on an effect of capillary elevation of wetting liquid into cracks due to a capillary pressure caused by a surface tension of the liquid [18]. Subsequently, the tested specimens were subjected to the Magnetic Particle inspection according to EN ISO 17638 used for the detection of surface defects in ferromagnetic materials. Magnetic field in defected locations appears above surface and creates a so-called Magnetic Scattering Flux. Magnetic poles are formed at edges of the cracks, and at the points where field lines leave a material and return to it again. Crack indication is formed by particles of detection medium (magnetic powder suspension 761 F) which are attracted by a scattering flux, see [19, 20].

DETERMINATION OF GEOMETRICAL PARAMETERS OF THE DEFECTS IN THE LASER CLADDED LAYERS BASED ON TOMOGRAPHICALLY OBTAINED DATA

Tomographical device TORATOM (Twinned Orthogonal Adjustable Tomograph) combines two pairs of X-ray tube-detector in an orthogonal arrangement with shared and a very precise rotation platform with a vertical axe of rotation which enable very specialized methods of collecting of tomographical data (dual source, dual energy), see Fig. 5.

The device has fully motorized axes to set a distance of X-ray tube - examined object - detector which allows a magnification from around 1.2× up to 100×. With a given pixel size of detector, it is possible to modify a resolution of CT reconstruction between 200 micrometers up to units of micrometers for a spatial point (voxel). In an addition to tomography, this device also enables a large-scale X-ray scanning of flat objects by gradual scanning of subsequent parts of examined object.

Steel sample was fixed in a rotation axis of tomographic table by using a chuck, see Fig. 5, item no. 4. The object was scanned by one pair of X-ray-detector. Due to a high decline of X-ray radiation in metal materials, XWT-240-SE (X-Ray WorX) microfocus X-ray tube was used as a source of X-ray radiation, which enables a using of an accelerating voltage of 230 kV at a target power of 50 W.

X-ray beam was filtered by a layer of brass with a thickness of 1.5 mm in order to remove photons of low energies which do not contribute to image information and cause a visual noise, or over excitation of detector outside an object. A flat panel with a GOS scintillator (XRD 1611, Varex Imaging) was used for a screening with an active area size of approximately 409.6×409.6 mm, a pixel matrix of 4096×4096, and a pixel size of 100 μm, operating at a capacity of 0.25 pF. The screening was done in 1080 angles of rotation of the object.

At each angle, an image (projection) was taken by averaging two images with 2×2 binning (avg) and with an exposure time of 2 s. The magnification was set to the highest possible reading due to the size of the investigated object and the active area by distances between the radiation source, the object and the detector while only a part of the sample with a height of 30 mm was monitored. Size of a spatial point (voxel) in a reconstructed model is approximately 16.7 micrometers at 12× magnification. For the projection correction, the "flat field correction" (FFC) method was used with a use of averaged radiographs from a scene without an object ("open beam") and without a radiation ("dark field"). For FFC, an average of 200 images with an exposure time of 2 s was used.

A serious adverse phenomenon when scanning metals is the influence of the so-called scattering, i.e. reflections and scattering of photons on the metal material - the edges of the object are blurred and the whole object is foggy. Another problem related to the high moderation of the measured metal is insufficient information inside the object and a phenomenon called beam hardening, i.e. a higher moderation of softer photons in the thickness of the material, which in the reconstruction causes an evident thinning of the internal structure of the material compared to the areas near the surface. VG Studio Max 3.4 software (Volume Graphics) was used to reconstruct the resulting virtual model. Due to the problems described above, algorithms were used during the reconstruction to suppress scattering and remove beam hardening. The result of the tomographic reconstruction is a three-dimensional matrix of voxels whose values are coded in 65535 shades of grey (UInt 16). The shades of grey correspond to the degree of moderation of X-ray radiation in the studied object, while the lighter the shade (higher value), the higher the moderation of X-ray radiation and vice versa.

In order to determine a damage depth as accurately as possible, the final tomographic models were first spatially transformed so that the tomographic sections in all flat surfaces were parallel to flat surfaces of the sample and the outer

edge of the deposit corresponded to a zero position on the Y axis. The "Porosity/Inclusion Analysis" module implemented in the previously mentioned VG Studio Max 3.4 software was used for a detection and segmentation of defects (non-integrities) in a cladded layer. The module is designed to examine 3D voxel arrays for internal imperfections such as voids and inclusions, and to provide detailed analysis results with information about each individual defect as well as overall statistical information. During the analysis, information such as a location, size, surface area, and volume of each individual defect can be obtained. First, each voxel in the monitored area ("region of interest", ROI) is checked, based on its value in a relation to the specified local contrast threshold, to see if it is part of the defect. Subsequently, groups of nearby voxels registered as defects are created.
Analysis incline to image noise, and in the presence of which there is a large number of false detections and a high consumption of calculation time. In order to suppress these problems and define the 6 defects as precisely as possible, an image filtering with a "non-local means" algorithm was used. This reduces the noise in the data set significantly, while preserving internal structures and edges.

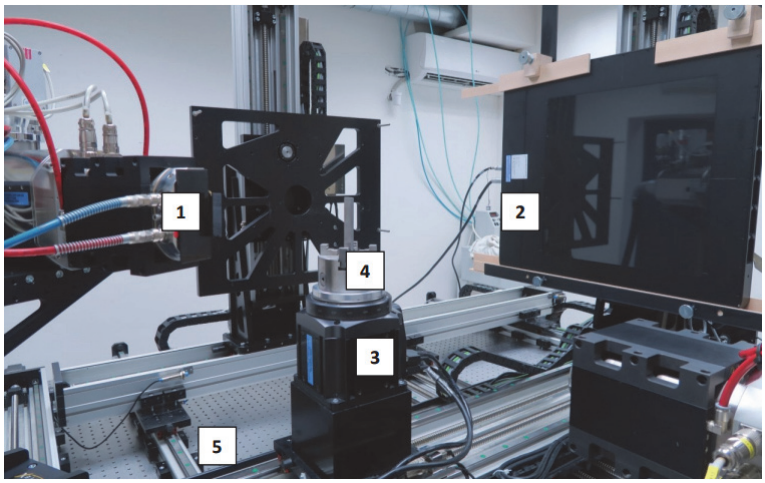

Figure 5: Photo of arrangement of the TORATOM tomograph during an irradiation of the studied samples; (1) X-ray tube XWT-240-SE; (2) flat panel detector XRD 1611; (3) high-precision rotary platform with a vertical axis of rotation; (4) chuck with an attached sample; (5) anti-vibration table with an active damping terminus of vibrations and CNC-controlled feeds component.

MECHANICAL THREE-POINT BENDING TEST

Three-point bending tests (21×5.5×100(80) mm) were applied to evaluate the impact of the laser cladded layers on the fatigue life of components made from the high strength steel S960. Cyclic loading causes initiation, cumulation and propagation of structural defects in the material. Plastic deformations and the initiation of fatigue cracks occur in places of stress concentration. This process leads to the growth of long fatigue cracks and can lead to fracture [21, 22]. The course and results of the three-point bending tests are dealt with in more profoundly in the work Fatigue life of S960 high strength steel with laser clad functional surface layers, see [7]. For the samples in which a series of tomographic measurements were performed, the influence of the detected structural defects on the final fracture was monitored and assessed.

RESULTS AND DISCUSSION

The non-destructive tests (Dye Penetrant Crack Test and Magnetic Particle Inspection) detected short open surface cracks only in the cladded aluminium bronze layer (sample No. B9/17). No surface defects were indicated by these methods in the other material samples.
In case of the tomographic analysis of defects, a region of interest (ROI) was defined in each sample. This area was chosen in the X- and Z-axis directions in the centre of the sample and slightly smaller than its boundaries to avoid false detection of the defects caused by artifacts at the steel/air interface. The size of the ROI in these two directions was constant, namely 5 mm in the direction of the X axis and 28 mm in the direction of the Z axis. The size of the area in the direction of the Y axis then varies depending on the thickness of the deposit layer, or the depth of the damage. All the parameters are summarized in the Tab. 3. An interval distribution of frequencies of the detected faults according to a length in the Y axis is shown in the Tab. 4 and the following graphs (Figs. 5-8).

Dimensions [mm]	Material (specimen number)			
	CuAl/S960 (B9/17)	Hard chrome/S960 (T34)	Cobalt alloy (ST9/14)	Stainless steel/S960 (N9/17)
Height W_{ROI}	28.00	28.00	28.00	28.00
Width B_{ROI}	5.00	5.00	5.00	5.00
Depth H_{ROI}	1.90	1.70	1.40	1.18
Thickness of the layer t	1.77	0.76	0.82	0.98
Maximum length of damage	0.61	0.58 (0.27)	0.12	0.27

Table 3: Parameters of the monitored area of interest ROI and a maximum detected length of fault in the Y axis.

Interval of length [mm]	Material (specimen number)			
	CuAl/S960 (B9/17)	Hard chrome/S960 (T34)	Cobalt alloy (ST9/14)	Stainless steel/S960 (N9/17)
(0.02, 0.08>	11	0	0	122
(0.08, 0.14>	9	41	22	110
(0.14, 0.20>	0	25	2	14
(0.20, 0.26>	0	3	0	7
(0.26, 0.32>	0	1	0	1
(0.32, 0.38>	1	1	0	0
(0.38, 0.44>	1	2	0	0
(0.44, 0.50>	1	0	0	0
(0.50, 0.56>	3	0	0	0
(0.56, 0.62>	1	0	0	0

Table 4: Interval distribution of frequencies of the detected defects according to a length in Y axis.

Aluminium bronze/S960 (B9/17) and Stainless steel/S960 (N9/17):
Both samples evince very distinct and sharply restricted damage. The sample B9/17 has approximately twice the thickness of the layer and approximately twice times the maximum length of the defects presented than the sample N9/17 where fewer defects (about ten times) were detected, however smaller ones. The samples have a comparable porosity of the monitored areas of the deposit – 0.3% for B9/17 and 0.26% for N9/17. It is clear to see that in the sample B9/17, the damage appears almost exclusively to a depth of 0.6 mm and is often connected with the surface. On the contrary, the sample N9/17 has very little surface damage, but a large number of the defects can be found both between the individual layers of the coating and also at the border between the coating and the substrate, see Figs. 9 and 10.

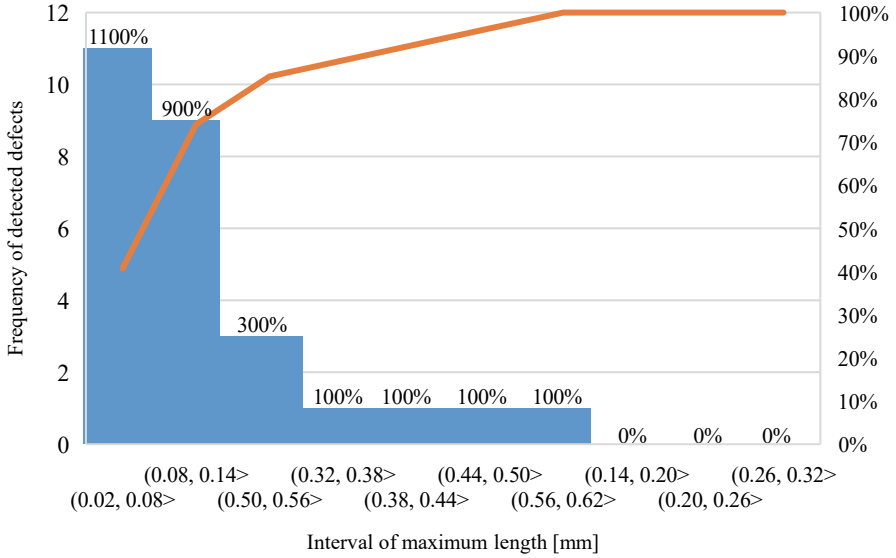

Figure 5: Distribution of frequency of defects detected in sample B9/17.

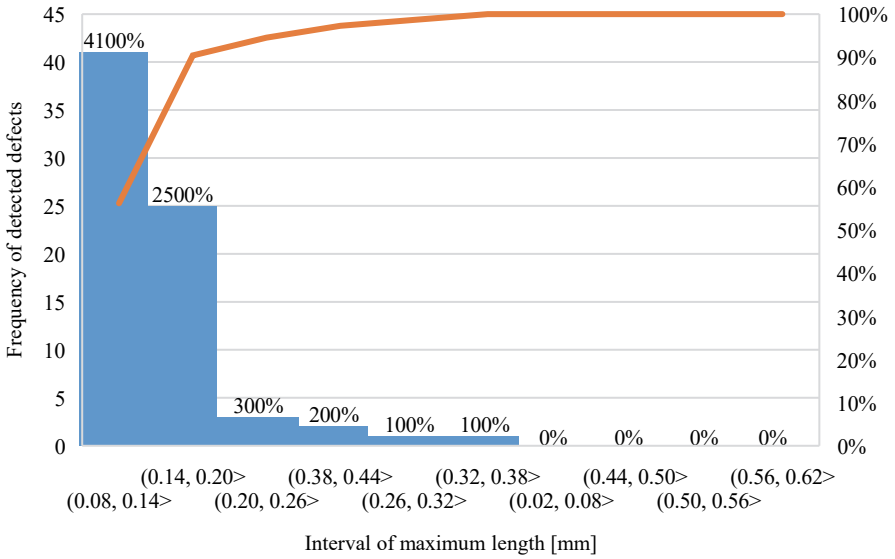

Figure 6: Distribution of frequency of defects detected in sample T34

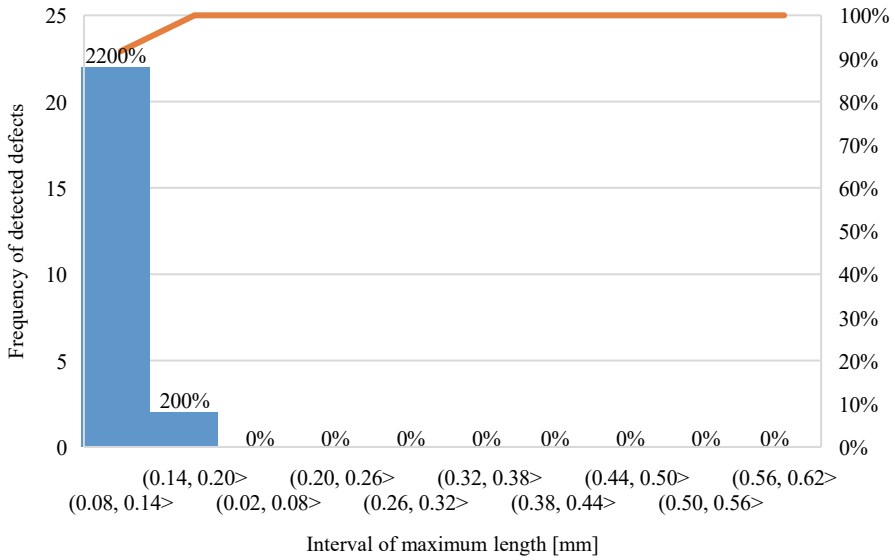

Figure 7: Distribution of frequency of defects detected in sample ST9/14

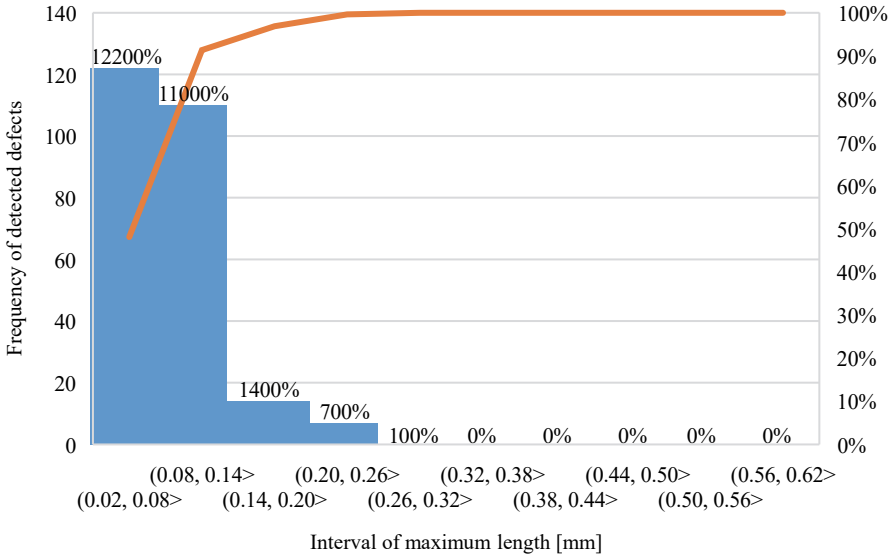

Figure 8: Distribution of frequency of defects detected in sample N9/17

Hard chrome / S960 (T34):

In this specimen, the damage apparently extends into a layer which is deeper than the thickness of the coating. This fact can be observed better on the side section (in the YZ plane, see Fig. 11). It was found that the three largest failures registered at the interface between the cladding layer and the substrate for the T34 sample with the lengths of 0.58, 0.36 and 0.33 mm occur precisely in the steel substrate and not in the coating itself. The longest crack in the coating has a length of 0.27 mm – in the results Tab. 3. An example of visualization of the tomographic section is shown in Fig. 12.

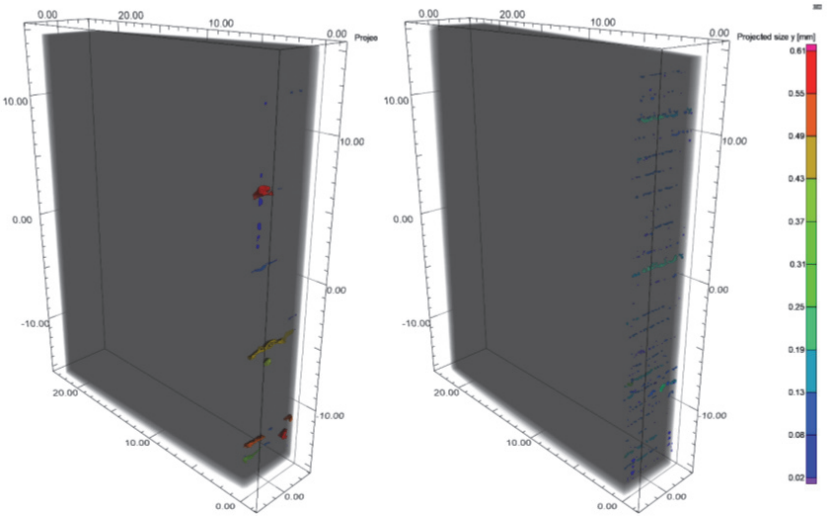

Figure 9: Three-dimensional representation of detected faults for the samples B9/17 (left) and N9/17 (right).

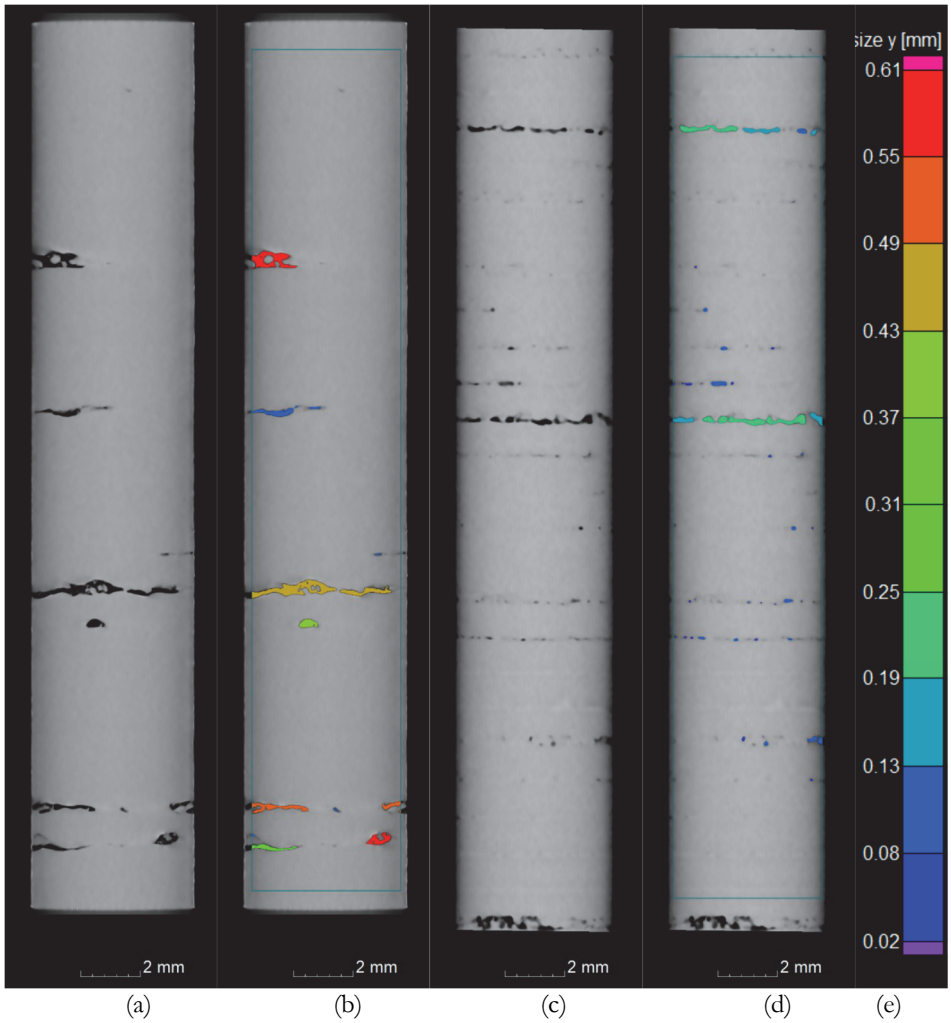

(a) (b) (c) (d) (e)

Figure 10: Visualization of the tomographic section of the sample B9/17 (a, b) and N9/17 (c, d) at a depth of approximately 0.3 mm. Plain sections by the tomographic reconstruction (a, c) and sections with the segmented damage (b, d) are shown, a color map of coding of the detected faults according to the length in the Y axis (e)

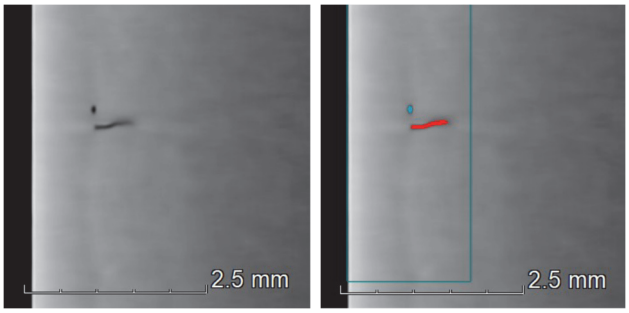

Figure 11: Zooming in on the side section of the largest crack registered with the T34 sample in the YZ plane. From the plain section (picture on the left) as well as the section after registration failure (picture on the right), it can be seen that the crack commences in the material interface and extends into the substrate.

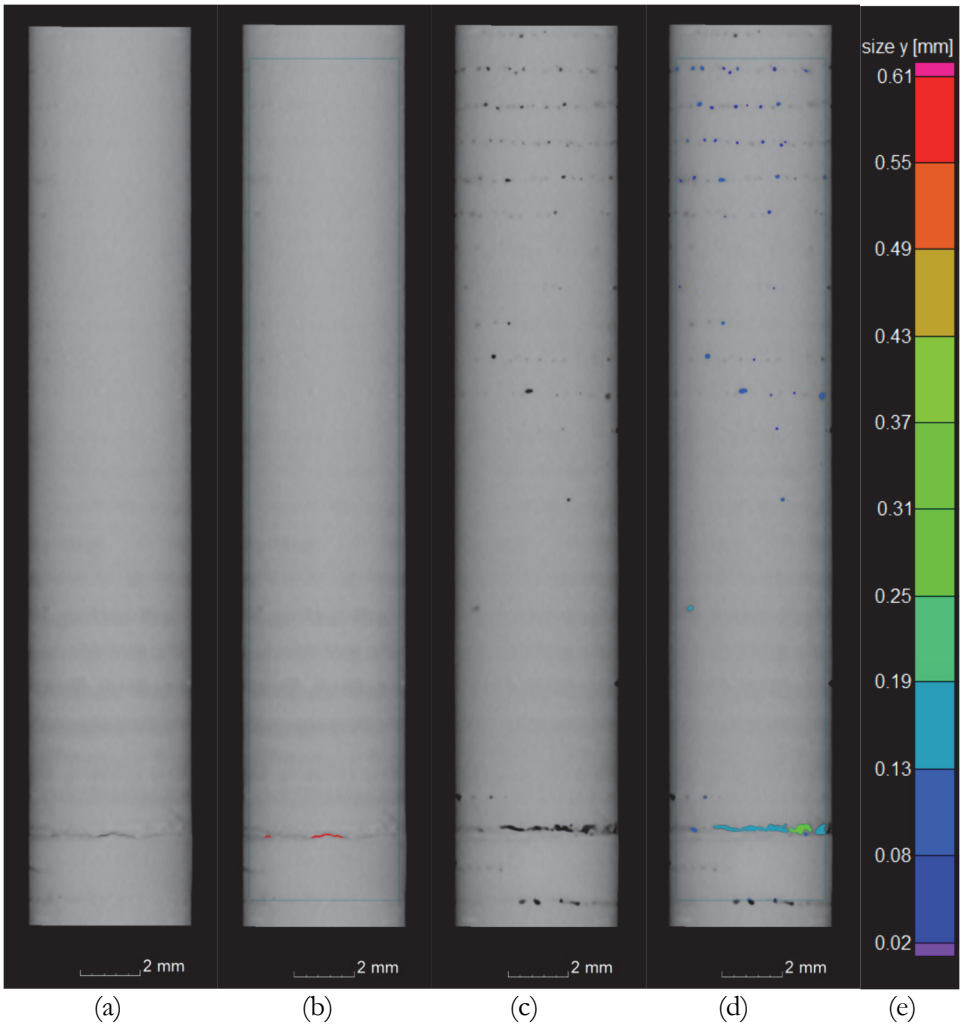

Figure 12: Visualization of tomographic section of the sample T34. Section behind the material interface at a depth of approx. 0.83 mm (a) the same section with segmented damage (b), section in the area of the transition layer at a depth of approx. 0.74 mm (c) the same section with segmented damage (d), color map of the coding of detected faults by Y-axis length (e)

Cobalt alloy/S960 (ST9/14)

The sample with the cobalt alloy deposit evince the smallest amount and size of segmented damage. But it is important to remember that cobalt alloy scatters X-ray radiation considerably more than steel, which means it's more susceptible to scattering than the other materials on offer. and is therefore burdened by scattering more than the other presented materials. Therefore, it cannot be excluded that there are more defects in the deposit. It was not possible to detect them tomographically especially due to the scattered photons. From the section in Fig. 13 (a), two overlap layers of the deposit can be traced.

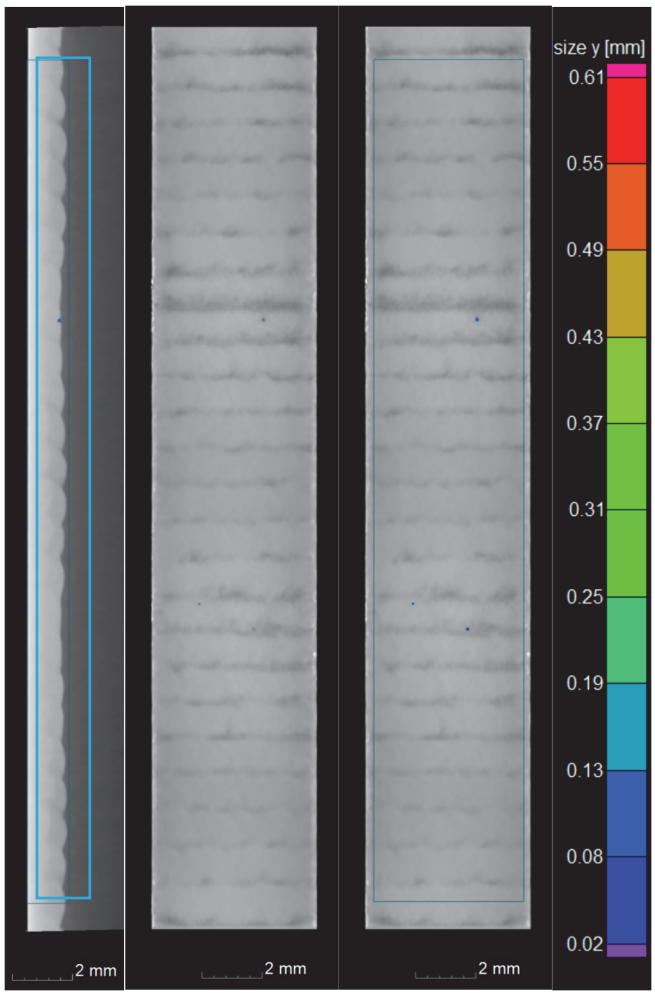

Figure 13: Visualization of tomographic section of the sample ST9/14. YZ plane side section (a) showing the boundary between the cladding layer and the substrate (the blue box represents the ROI boundaries), the section in the transition layer region (b) the same section with segmented damage (c), the color-coding map of the detected defects according to the axis length Y (d)

Samples with defined morphometric parameters of internal defects close to the bi-metal interface were included in a series of three-point bending tests and subsequently, the analysis of the microstructure of fractures using a scanning electron microscope Tescan LYRA 3 XMU FEG/SEMxFIB was performed. Properties of settings and measured values obtained from the three-point bending test are stated in Tab. 5.

Sample No.	W_0 [mm³]	M [Nm]	P_a [kN]	P_m [kN]	P_{max} [kN]	P_{min} [kN]	f [Hz]	σ_{max} [MPa]	σ_a [MPa]	N_f [cycles]
B9/17	466.63	93.33	2.000	2.444	4.444	0.444	76.90	200	90.0	10^7
T34	391.91	58.79	1.260	1.540	2.799	0.280	77.30	150	67.5	1,683,000
ST9/14	415.37	186.92	4.005	4.895	8.901	0.890	81.90	450	202.5	10^7
N9/17	415.99	124.80	2.674	3.269	5.943	0.594	80.30	300	135.0	3,496,416

Table 5: Properties of settings and measured values for the three-point bending tests.

More than 10^7 cycles were performed for samples B9/17 and ST9/14 as you can see in the Tab. 5. For specimen B9/17 it was 17,760,000 cycles to failure and for specimen ST9/14 then 14,138,000 cycles. In sample B9/17, the final crack was most likely initiated at the interface of two overlapping surface layers in a relative depth of more than 500 µm. Due to the rather superficial nature of the detected cracks with the maximum depth of around 0.6 mm can be assumed that none of the cracks detected in this sample significantly affected the fatigue life during the three-point bending test. The situation is similar for sample ST9/14. The dominant crack leading to the rupture of the specimen was most likely initiated from the surface. No open surface cracks were identified by any of the methods that were applied to detect surface cracks. Also, the tomographically obtained data do not indicate the occurrence of subsurface defects with

connections to the surface. It can be assumed that even in this case the service life of the sample was not affected due to the detected structural non-integrities.
The situation is different for sample T34. Despite the used lower maximum stress σ_{max}, the sample fractured after significantly fewer load cycles than the previous two samples. This is the sample with the greatest number of observed defects. Multiple crack initiation was detected at the interface of the two layers in the region of predicted critical crack development leading to fatigue fracture. From the above it can be therefore assumed that the location, length and frequency of defects had an effect on the fatigue life of the sample. On the contrary, the effect of cracks detected in the base material was not proven.
Bigger number of defects were tomographically also detected in sample N9/17 especially near the interface of the first surface layer and the base material. There was observed multiple initiation of cracks, leading to the development of a critical crack and fatigue fracture in the same area during an analysis after performing the three-point bending test. It can be supposed that the observed defects affected the fatigue behaviour of the sample.

Conclusion

Based on the submitted information and results plotted in the tables (Tabs. 1-5) and figures (Figs. 1-13) above, the following statements can be concluded:

- X-ray micro-tomography was performed and the data obtained were processed in the sense of non-descrutive, segmentation and determination of geometric parameters of the present defects. The achieved spatial point size of the obtained models (voxel) was approximately 16.7 micrometres. The defects with a volume greater than 8 voxels were observed. In all samples, the small defects were detected and subsequently segmented. Their length in the observed direction (perpendicular to the surface of the coating) was in the range of 20-610 micrometres. Some of the cracks in specimen T34 (hard chrome) were shown to extend into a layer deeper than the thickness of the coating, i.e. into the steel substrate.
- The solidified grain size and shape in the cladding zone show non-uniformity because of variations in nucleation and growth circumstances. The grain shape in the cladding layer varies between columnar and equiaxed crystals as one moves from the bottom to the top.
- The three-point bending tests have been performed. Fatigue fractures were analysed by electron microscope and evaluated. It can be concluded that the used technology, heat effects, the quality of the metallurgical bond, the frequency and location of defects in the cladded structure, negatively affect the fatigue behaviour, see samples T34 and N9/17. On the other hand, the presence of inhomogeneities/defects in the surface layer does not always necessarily lead to the development of these defects into a main crack leading to fatigue fracture and affect the durability of the product/component. In samples B9/17 and ST9/14, microstructural short cracks initiated and propagated in places where no significant defects were detected tomographically.
- It is important to have a good knowledge about the effect of internal defects in surface layer and in the area of the bi-material interface on the initiation and propagation of fatigue cracks and thus on the fatigue behaviour of the component.

It should be noted that the results presented within this paper are a part of the investigation 'Fatigue behaviour of metallic components with bi-material interface', see [7][17][23][24]. These pilot results are going to be complemented by additional studies such as for example x-ray microtomography investigation combined with four-point bending test implemented to multiple samples of same material groups.

Acknowledgements

This paper was created as a part of the project No. CZ.02.01.01/00/22_008/0004631 "Materials and technologies for sustainable development" within the Jan Amos Komenský Operational Program financed by the European Union and from the state budget of the Czech Republic. Financial support from the Faculty of Civil Engineering, Brno University of Technology (project No. FAST-S-24-8503) and from the Czech Science Foundation (project No. 21-14886S) is also gratefully acknowledged.

Data Availability

The data used in this study is available at: DOI: 10.5281/zenodo.13897315

REFERENCES

[1] Xu, J.S., Zhang, X.C., Xuan, F.Z., Tian, F.Q., Wang, Z.D., Tu, S.T. (2013). Tensile properties and fracture behavior of laser cladded WC/Ni composite coatings with different contents of WC particle studied by in-situ tensile testing, Mater. Sci. Eng. A, C(560), pp. 744–751, DOI: 10.1016/J.MSEA.2012.10.028.

[2] Chen, Y., Guo, Y., Xu, M., Ma, C., Zhang, Q., Wang, L., Yao, J., Li, Z. (2019). Study on the element segregation and Laves phase formation in the laser metal deposited IN718 superalloy by flat top laser and gaussian distribution laser, Undefined, 754, pp. 339–347, DOI: 10.1016/J.MSEA.2019.03.096.

[3] Konieczny, M. M., Achtelik, H., Gasiak G. (2021) Influence of the applied layer on the state of stress in a bimetallic perforated plate under two load variants, Frattura ed Integrità Strutturale, 56, pp. 137–150, DOI: 10.3221/IGF-ESIS.56.11.

[4] Motarjemi, A., Koçak, M., Ventzke, V., (2002). Mechanical and fracture characterization of a bi-material steel plate. International Journal of Pressure Vessels and Piping 79 (3), pp. 181–191, DOI: 10.1016/S0308-0161(02)00012-1

[5] Bhat, S., Adarsha, H., Ravinarayanr, V., Koushik, V.P. (2019) Analytical model for estimation of energy release rate at mode I crack tip in bi-material of identical steels joined by an over-matched weld interlayer. Procedia Structural Integrity 7, pp. 21–28, DOI: 10.1016/j.prostr.2019.08.004.

[6] Konmanová, L., Haušild, P., Materna, A., Matějíček, J. (2015) Investigation of Indentation Parameters Near the Interface between Two Materials. Key Engineering Materials, 662, pp. 31–34, DOI: 10.4028/www.scientific.net/KEM.662.31.

[7] Doubek, P., Kozáková, K., Kunz, L. and Seitl, S. (2024) Fatigue life of S960 high strength steel with laser cladded functional surface layers, Eng. Fail. Anal., 164, pp. 108629, DOI: 10.1016/j.engfailanal.2024.108629.

[8] Morel, F., Guerchais, R., and Saintier, N. (2015). Competition between microstructure and defect in multiaxial high cycle fatigue. Frattura Ed Integrità Strutturale, 9(33), pp. 404–414. DOI: 10.3221/IGF-ESIS.33.45.

[9] Fíla, T., Vavřík, D. A multi-axial apparatus for carrying out X-ray measurements, particularly computed tomography. European patent No. 14002662.6.

[10] Kumpová, I., Rozsypalová, I., Keršner, Z. Rovnaníková, P., Vopálenský, M. (2019) X-ray micro-tomography characterization of voids caused by three-point bending in selected alkali-activated aluminosilicate composite. In Acta Polytechnica CTU Proceedings 25: 17th Youth Symposium on Experimental Solid Mechanics. 25. Prague, pop. 58–63. ISBN: 978-8-0010-6670-6.

[11] Seitl, S., Al Khazali, M., Malíková, L. (2024) Appropriate cumulative fatigue damage models for fatigue life estimation applied to high-strength steels. Kovové materiály - Metallic Materials, 62, pp. 41–51, DOI: 10.31577/km.2024.1.41.

[12] Laser Therm s.r.o. Homepage – Laser Therm s.r.o. [online, 8.5.2022]. https://www.lasertherm.cz/eng/technologies/laser-technologies/laser-cladding.

[13] Sartika, V.D., Choi, W.S., Choi, G., Han, J., Chang, S.-J., Ko, W.-S., Grabowski, B. and Choi, P.-P. (2022) Joining Dissimilar Metal of Ti andCoCrMo Using Directed Energy Deposition. J. Mater. Sci. Technol. 111, pp. 99–110 DOI: 10.1016/j.jmst.2021.09.038.

[14] Siddiqui, A.A., Dubey, A.K. (2021) Optimization of geometrical and mechanical characteristics in laser surface alloying, Materials Today: Proceedings,44(1), pp. 1108–1110, DOI: 10.1016/j.matpr.2020.11.186.

[15] Potts, P. J., Webb, P. C. (1992) X-ray fluorescence spectrometry, Journal of Geochemical Exploration 44, pp. 251–296, DOI: 10.1016/0375-6742(92)90052-A.

[16] Bonvin, D., Yellepeddi, R. (2009). Latest developments in X-ray fluorescence spectrometry and X-ray diffraction technology for iron and steel industry: Integrated chemical and phase analysis. 29, pp. 1–6.

[17] Doubek, P.; Malíková, L.; Miarka, P.; Seitl, S. (2023) Laser cladded protective layer on the S960 Change of microhardness in the vicinity of the bi-material interface, Procedia Structural Integrity, 43, pp. 101–106, DOI: 10.1016/j.prostr.2022.12.242.

[18] Ness, S. (1996) Nondestructive Testing Handbook Vol. 10, Nondestructive Testing Overview, American Society for Nondestructive Testing, pp. 76.

[19] Betz, C.E. (1988). Principles of Magnetic Particle Testing, Magnaflux Corporation, American Society for Non-destructive Testing.

[20] Qiang Wu, Kang Dong, Xunpeng Qin, Zeqi Hu, Xiaochen Xiong; (2024) Magnetic particle inspection: Status, advances, and challenges-Demands for automatic non-destructive testing. NDT & E International, 143, pp. 103030, DOI: 10.1016/j.ndteint.2023.103030.

[21] Pook, L. (2007) Metal fatigue. New York: Springer-Verlag New York Inc. pp. 271, ISBN 140205596X

[22] Belan, J., Kuchariková, L., Tillová, E., Chalupová, M. (2019) Three-Point Bending Fatigue Test of TiAl6V4 Titanium Alloy at Room Temperature", Advances in Materials Science and Engineering, pp. 2842416, DOI: 10.1155/2019/2842416.

[23] Malíková, L., Miarka, P., Doubek, P., Seitl, S. (2022) Influence of the interphase between laser-cladded metal layer and steel substrate on the fatigue propagation of a short edge crack. Frattura ed Integrita Strutturale, 59, pp. 514–524, DOI: 10.3221/IGF-ESIS.59.33.
[24] Malíková, L., Miarka, P., Doubek, P., Seitl, S. (2021) Influence of the bi-material interface on the crack propagation through a thin protective layer. Procedia Struct. Integr. 33, pp. 605–612, DOI: 10.1016/j.prostr.2021.10.067.